Journal of ELECTRONIC MATERIALS, Vol. 44, No. 1, 2015
DOI: 10.1007/s11664-014-3457-y

Comparison of CVD- and MBE-grown GaN Nanowires: Crystallinity, Photoluminescence, and Photoconductivity

R.S. CHEN,[1,6] H.Y. TSAI,[2] C.H. CHAN,[3] Y.S. HUANG,[3] Y.T. CHEN,[4] K.H. CHEN,[4] and L.C. CHEN[5]

1.—Graduate Institute of Applied Science and Technology, National Taiwan University of Science and Technology, 43, Sec. 4, Keelung Rd, Taipei 10607, Taiwan. 2.—Graduate Institute of Electro-Optical Engineering, National Taiwan University of Science and Technology, Taipei 10607, Taiwan. 3.—Department of Electronic Engineering, National Taiwan University of Science and Technology, Taipei 10607, Taiwan. 4.—Institute of Atomic and Molecular Sciences, Academia Sinica, Taipei 10617, Taiwan. 5.—Center for Condensed Matter Sciences, National Taiwan University, Taipei 10617, Taiwan. 6.—e-mail: rsc@mail.ntust.edu.tw

The crystalline quality, photoluminescence (PL), and photoconductivity (PC) of gallium nitride (GaN) nanowires (NWs) grown by chemical vapor deposition (CVD) and molecular beam epitaxy (MBE) have been investigated and compared. The common single-crystalline structures and distinct long-axis orientation are confirmed for the CVD (m-axial) and MBE (c-axial)-GaN NWs. The PL examination reveals the difference of crystalline quality of the GaN NWs, which is difficult to differentiate by structural characterization methods. The MBE-grown NWs show sharper band-edge emission and much less defect emission in comparison to the CVD-grown NWs. However, it is interesting that the CVD-GaN NWs exhibit much higher photocurrent generation efficiency (or normalized gain) than those grown by MBE. The probable physical origins, including carrier concentration, surface state density, and surface polarity, that induce different surface band bending for PC, have also been proposed and discussed. The environment-dependent photoconductivities under inter-bandgap and sub-bandgap excitations were also observed. The systematic study concludes that the PL and PC behavior of this nitride nanostructure are controlled by two different mechanisms in the bulk and surface, respectively.

Key words: Gallium nitride, nanowire, photoconductivity, photoluminescence, chemical vapor deposition, molecular beam epitaxy

INTRODUCTION

Over the past two decades, the quasi one-dimensional (1D) nanostructures, such as nanowires (NWs) and nanorods, of gallium nitride (GaN) have attracted intense attention of the researchers in the fields of photonics, electronics, optoelectronics, semiconductor physics, and material sciences.[1–11] In addition to the inherent advantages of GaN such as wide direct bandgap (~3.4 eV), high optical absorption coefficient, high electron mobility, physical and chemical robustness, and bio-compatibility,[12–17] its NW with size-confined geometry, anisotropic path for carrier transport, and high surface-to-volume ratio further provide the motivation for research and boost the development of devices. To prepare the high-quality GaN nanocrystals, two major growth techniques including chemical vapor deposition (CVD)[18–20] and molecular beam epitaxy (MBE)[21–24] have been applied. The studies of the fundamental properties and applications of the GaN NWs are usually based on one specific growth method. Although both the CVD and MBE approaches have

(Received April 28, 2014; accepted October 3, 2014; published online October 25, 2014)

been demonstrated to produce very high-quality GaN NWs with single-crystallinity, understanding the differences of the material properties between CVD- and MBE-grown NWs could be an interesting and useful issue.

Especially, photoconduction (PC) properties in this nitride 1D nanostructure have been confirmed to be dominated by the surface. The mechanism of electron–hole spatial separation induced by surface band bending (SBB) in the GaN NWs provides an excellent carrier collection efficiency and extremely high gain which is several orders of magnitude higher than the conventional thin film and bulk counterparts.[25–33] The surface-controlled properties also motivated the usage of GaN NWs as the gaseous and biological sensors.[10,34–36] A comparison of inherent PC efficiencies for CVD- and MBE-grown GaN NWs was made in our previous report.[32] The CVD-GaN NWs exhibited higher photocurrent generation efficiency than the MBE ones. In this paper, we will further investigate and compare the structural and photoluminescence (PL) properties of the CVD- and MBE-GaN NWs in addition to their photoconductivities. The differences of the material properties and their physical mechanisms dominated either by the surface or by the bulk will be discussed systematically.

EXPERIMENTAL

The GaN NWs used for PC measurements were respectively grown by thermal CVD and radio frequency plasma-assisted MBE. For CVD growth, a nanometer-thick Au film was pre-coated on the silicon substrate as the catalyst. The metal catalyst was not necessary for MBE growth but the Si(111) substrate was used for the aligned growth of GaN NWs. More details of the material growth can be found in our earlier publications.[2,20,24] The morphologies, structures, and crystalline qualities of the GaN NWs were characterized by field-emission scanning electron microscopy (FESEM), x-ray diffractometry (XRD), Raman spectroscopy, high-resolution transmission electron microscopy (HRTEM), selected-area electron diffractometry (SAD) and PL spectroscopy at room temperature.

The two-terminal devices of the individual GaN NWs were fabricated by two different methods. The devices of CVD-NWs with long enough lengths were fabricated by the shadow-mask (SM) approach using Ti(30–50 nm)/Au(50–150 nm) as the bilayered contact electrode.[37] The MBE-GaN NWs with shorter lengths (2–6 μm) were fabricated by focused-ion beam deposition (FIB, FEI Quanta 3D FEG) using Pt as the contact metal.[38] The detailed parameters of the individual NW devices used for PC measurements are listed in Table I.

Electrical measurements were carried out on an ultralow current leakage cryogenic probe station (LakeShore Cryotronics TTP4). A semiconductor characterization system (Keithley 4200-SCS) was utilized to source dc bias and measure current. The He-Cd laser with 325 nm wavelength was used as the excitation source for the power and temperature-dependent PC measurements. The Nd:YAG and diode lasers were used to source 532 and 808 nm wavelength lights for sub-bandgap excitation. The incident power of laser was measured by a calibrated power meter (Ophir Nova II) with a silicon photodiode head (Ophir PD300-UV). A UV holographic diffuser was used to broaden laser beam size ($\sim$20 mm^2) to minimize the error of the power density calculation.

Fig. 1. The FESEM images of (a) the CVD- and (b) the MBE-grown GaN NW ensembles. (c) The XRD patterns and (d) the Raman spectra of the CVD- and MBE-GaN NW ensembles. The TEM and HRTEM images and their corresponding SAD patterns of (e, g) the CVD- and (f, h) the MBE-grown GaN NWs. The zone axes of the SAD patterns for the CVD-NW in 1 (g) and MBE-NWs in 1 (h) are $\langle 001 \rangle$ and $\langle 1\bar{1}0 \rangle$, respectively. ▶

RESULTS AND DISCUSSION

Morphology, Structure, and Crystallinity

The FESEM images of the GaN NW ensembles grown by CVD and MBE are depicted in Fig. 1a and b, respectively. The micrographs show the GaN NWs grown by catalyst-assisted CVD with much longer length ($>$20 μm) and spaghetti-like morphology, which is different from the vertically aligned NWs on Si(111) substrate grown by MBE. The diameter (d) distributions of the as-grown CVD- and MBE-NWs

Table I. The parameters including NW diameter (d), interdistance between two contact electrodes (l), and applied voltage (V), of the individual GaN NW devices for the photoconductivity measurements

Sample no.	d (nm)	l (μm)	V(V)	Long axis	Catalyst	Growth
# CVD-1	60 ± 10	16.9	0.5	m-axis	Au	CVD
# CVD-2	130 ± 15	11.3	0.02	m-axis	Au	CVD
# MBE-1	82 ± 12	1.1	0.1	c-axis	None	MBE
# MBE-2	110 ± 30	1.0	0.1	c-axis	None	MBE
# MBE-Ref[a]	65 ± 15	0.4	3.0	c-axis	None	MBE

The parameters of the MBE-GaN NWs taken from Ref. 28 are also listed.[a]Ref. 28.

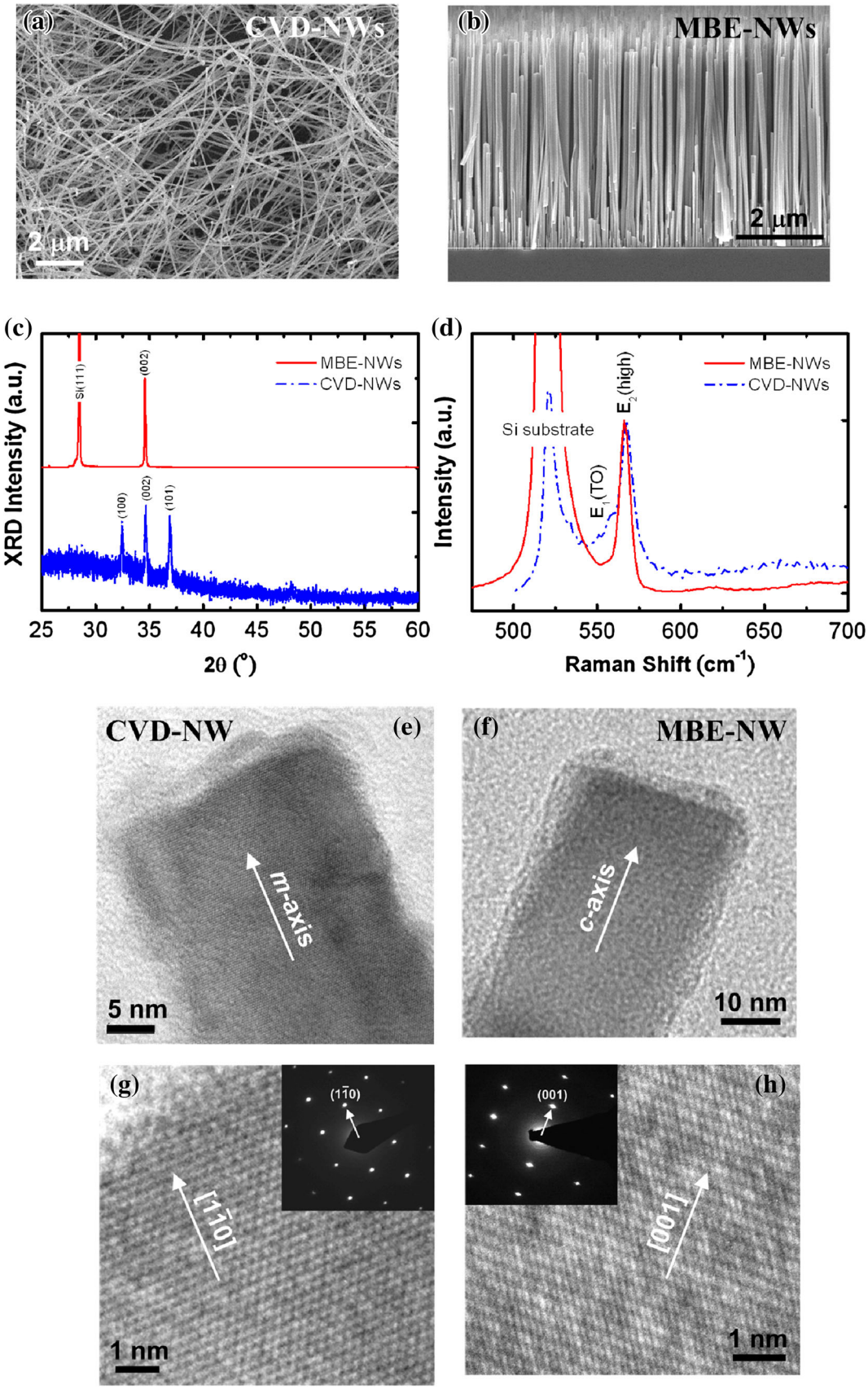
(a)
CVD-NWs
2 μm
(b)
MBE-NWs
2 μm
(c)
MBE-NWs
CVD-NWs
Si(111)
(002)
(100)
(002)
(101)
XRD Intensity (a.u.)
2θ (°)
(d)
MBE-NWs
CVD-NWs
Si substrate
E1(TO)
E2(high)
Intensity (a.u.)
Raman Shift (cm-1)
CVD-NW
(e)
m-axis
5 nm
(f)
MBE-NW
c-axis
10 nm
(g)
(1$\bar{1}$0)
[11$\bar{2}$0]
1 nm
(h)
(001)
[0001]
1 nm

are 20–160 nm and 50–200 nm, respectively. The common hexagonal wurtzite structure of the CVD- and MBE-GaN NW ensembles was confirmed by the XRD measurement as shown in Fig. 1c. The predominant (002) diffraction signal also shows the MBE-grown NWs with *c*-axial out-plane growth orientation and vertical alignment. The Raman spectra (Fig. 1d) of the CVD- and MBE-NW ensembles shows the major peak at ~566 cm^{-1}, which is attributed to the phonon mode of E_2(high) (569 ± 1 cm^{-1}) of the hexagonal GaN bulk crystals.[39–41] As the linewidth of the E_2(high) peak could be influenced by the phonon confinement effect in these nanostructures,[42] the peak broadenings were not used to compare the crystalline quality of the CVD- and MBE-NWs. In addition, Fig. 1e–h depict the TEM images and their corresponding SAD patterns, indicating the common single-crystalline structure and the different long-axial orientation along ⟨1$\bar{1}$0⟩ (*m*-axis) and ⟨001⟩ (*c*-axis) for the CVD- and MBE-GaN NWs, respectively. The HR-TEM images also reveal the clear lattice images of the monocrystalline GaN NWs grown by CVD (Fig. 1g) and MBE (Fig. 1h).

Photoluminescence

Although the structural characterizations by XRD, Raman scattering, HRTEM, and SAD have indicated the GaN NWs prepared by CVD and MBE with the single crystallinity in common, PL measurements were performed to the NW ensembles to differentiate the quality of the NWs prepared by the two different methods. Figure 2 illustrate the normalized PL spectra for the CVD- and MBE-GaN NWs. The linear scale plot in Fig. 2a reveals the major bandgap emission (at ~3.4 eV) of the CVD-NWs with broader linewidth than that of the MBE ones. The full-width at half maximum (FWHM) of the bandgap emission for the CVD-GaN NWs at ~200 meV is three times higher than that at 66 meV for the MBE-NWs. The result clearly indicates the superior crystalline quality of the MBE-grown NWs in comparison to the CVD-NWs.

Furthermore, the CVD-NWs also reveal significant defect band emission in the energy range of 1.5–3.0 eV. By taking the semi-logarithmic plot of the PL spectra in Fig. 2b, the defect emission can also be observed for the MBE-NWs. However, the intensity of the defect band emission (I_{DB}) is much lower than that of the bandgap emission (I_{BG}). While quantifying the ratio of I_{BG} to I_{DB} by taking their integrating intensity, the MBE-GaN NWs with much stronger band edge emission reveal the I_{BG}/I_{DB} ratio at ~60 which is remarkably higher than that at 1.3 of the CVD-NWs. The analysis further manifests the much less defect density and better crystalline quality in the MBE-GaN NWs compared to the CVD ones.

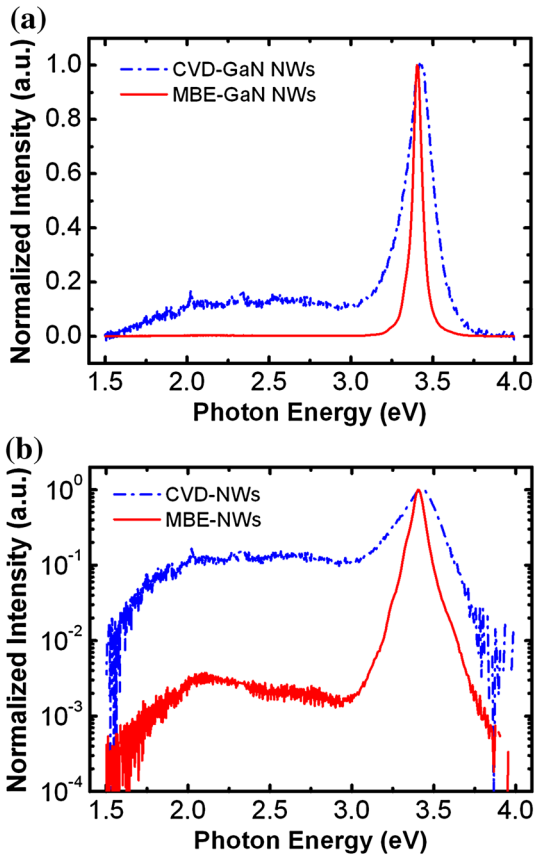

Fig. 2. The PL spectra of the CVD- and the MBE-grown GaN NWs plotted (a) by linear scale and (b) by semi-logarithmic scale.

Photoconductivity

Ohmic Contact Characterization

In addition to the structure and PL characterization, the transport properties of the individual GaN NWs will also be investigated and compared. Figure 3a and b illustrates the dark current (i_d) versus applied bias (V) measurements and the representative FESEM images (insets) for the single-wire devices of the CVD- and MBE-GaN NWs, respectively. The linear curve shows the good ohmic contact condition between the metal electrode and the semiconductor NW for either CVD- or MBE-NW devices. The difference between the slopes of the i_d–V curve (i.e. conductance (G)) is mainly due to the different dimensions of the NW devices as $G = \sigma(\pi r^2/l)$ under the columnar NW assumption, where σ is the conductivity, r is the NW radius, and l is the inter-distance between two metal electrodes. By taking r (= d/2) and l into account, the calculated σ for the CVD- and MBE-NWs are close and are in the range of 100–300 $\Omega^{-1}cm^{-1}$. The required parameters for the σ estimation of the NW devices are listed in Table I.

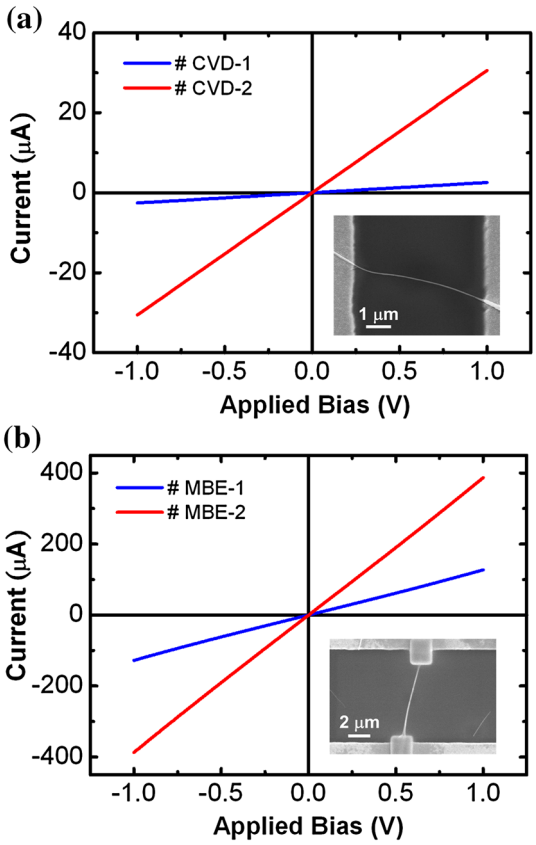

Fig. 3. The dark current versus applied bias (i_d-V) measurements for the single-NW devices with the GaN NWs grown by (a) the CVD and (b) the MBE approaches. The typical FESEM images of the CVD- and MBE-GaN NW devices are depicted in the insets of (a) and (b), respectively (Color figure online).

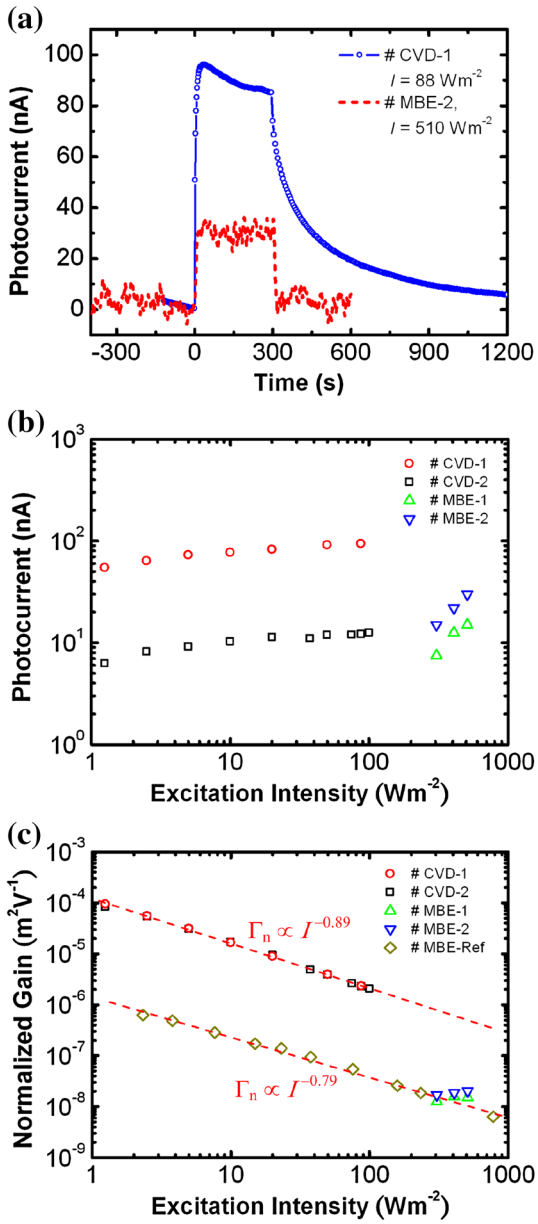

Fig. 4. The typical photocurrent response curves under one long pulse UV illumination (λ = 325 nm) for the CVD- and MBE-GaN NWs. (b) The steady-state photocurrent and (c) the normalized gain versus light intensity for the CVD- and MBE-grown GaN NWs. The data points taken from the MBE-GaN NWs in Ref. 28 are also plotted for comparison. The parameters of the individual GaN NW devices for the photoconductivity measurements are listed in Table I. The red dashed lines in (c) are the guiding lines by eyes to present the trends of the normalized gain versus intensity for the CVD- and MBE-NWs (Color figure online).[32]

Photoconduction Efficiency and Normalized Gain

The typical photocurrent responses under a long pulse excitation by the wavelength (λ) of 325 nm for the CVD (sample# CVD-1) and MBE (sample# MBE-2)-grown GaN NWs are depicted in Fig. 4a. As a relatively high light intensity ($I > 300$ Wm^{-2}) is required to generate observable photoresponse for the MBE-NWs, the photocurrent of the MBE-GaN NW under a higher I at 510 Wm^{-2} is still lower than that of the CVD-NW at I = 88 W m^{-2}. To have a clear picture, the values of the steady state photocurrent (i_p) under different excitation power density for the CVD- and MBE-NWs are summarized in Fig. 4b. Overall, the CVD-NWs reveal higher i_p and much lower detection limit of light power in comparison to the MBE ones. The value of i_p depends on the intrinsic material properties and experimental parameters. To understand the inherent difference of the PC performances of the GaN NWs grown by the different techniques, the physical origin of the i_p has to be investigated.

As i_p generation is a two-step process including optical absorption (determined by the net quantum efficiency (η)) and photocarrier collection (determined by photoconductive gain (Γ)), the i_p is written as.[43–45]

$$i_p = \frac{q}{E} P \eta \Gamma, \quad (1)$$

where q is the elementary charge, E is the photon energy, P is the incident optical power on the projected area ($A = dl$) of the measured NW and can be

calculated as $P = Idl$. Among the parameters, Γ plays the key role on the carrier collection efficiency and i_p value. Γ is a function of multiple parameters including carrier lifetime (τ), mobility (μ), V, and l, which can be expressed as $\Gamma = \frac{\tau}{\tau_t} = \tau\mu\frac{V}{l^2}$. Accordingly, Γ depends on both intrinsic property of material (i.e. τ and μ) and experimental parameters (i.e. V and l). Γof the photodetector devices can be directly improved by increasing V and shortening l, so Γ is a device-oriented quantity. More discussion on the Γ of the GaN NW photodetectors can be found in our previous report.[32] However, to understand the inherent differences between the CVD- and MBE-GaN NWs that results in the difference of PC efficiency or i_p, the artificial effects of V and l have to be excluded.

Accordingly, the normalized gain (Γ_n) defined as the product of η, τ, and μ (i.e. $\Gamma_n = \eta\tau\mu$) is adopted to determine the PC efficiency of the NW photoconductors.[46–48] As $\tau\mu$ product is an intrinsic quantity deciding carrier transport efficiency,[49] for a constant η, the Γ_n has the same physical meaning as $\tau\mu$, and its intrinsic property can rule out the contributions of material dimension and experimental condition. Γ_n taking η into account could also reflect the difference in practical light absorption efficiency

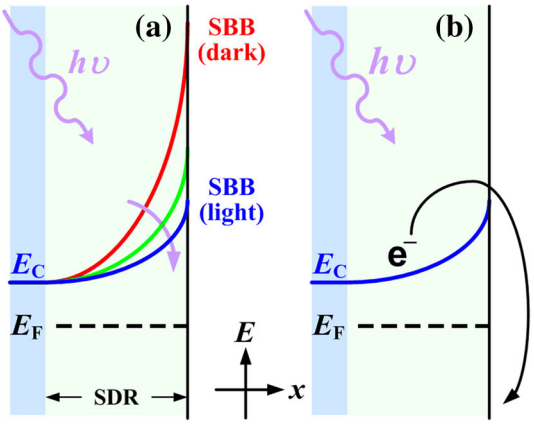

Fig. 5. Schematic illustration of (a) the decrease of surface band bending (SBB) in the surface depletion region (SDR) by light illumination due to the photovoltaic effect and (b) the mechanism of electron to overcome potential barrier under light illumination to recombine with hole or surface states by thermionic emission.

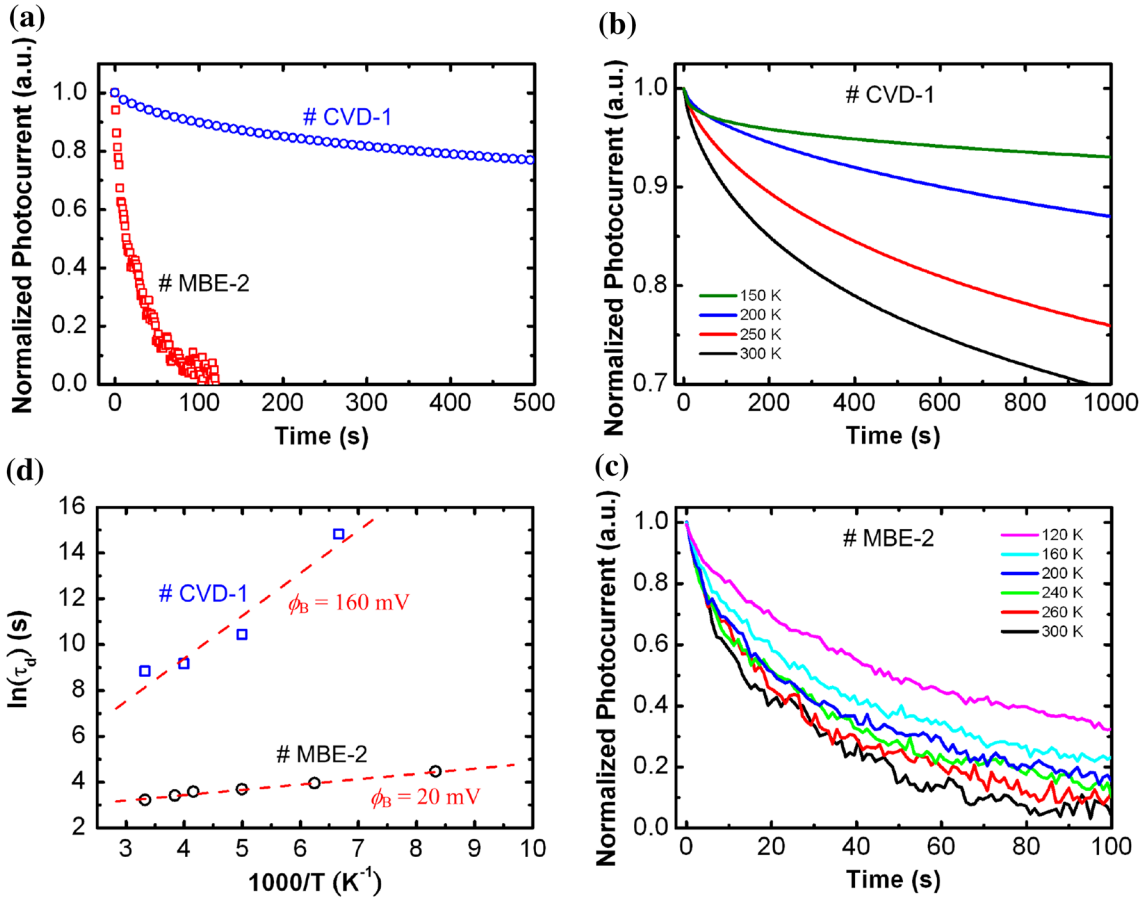

Fig. 6. (a) The comparison of the normalized photocurrent decay curves of the CVD- and MBE-GaN NWs. The temperature-dependent photocurrent decay measurements for (b) the CVD-GaN NW (sample# CVD-1) and (c) the MBE-GaN NW (sample# MBE-2). (d) The Arrhenius plots for the fitted decay time versus temperature curves for the CVD- and MBE-GaN NWs. The red dashed lines are the fitting curves to the data points (Color figure online).[32]

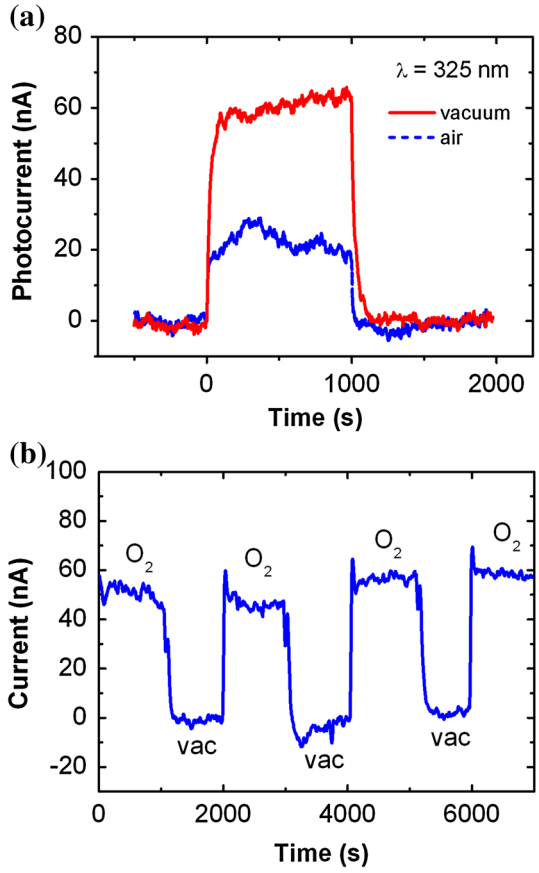

Fig. 7. (a) The photocurrent response curves under the inter-band-gap excitation at λ = 325 nm and I = 510 Wm^{-2} for the MBE-GaN NWs (sample#MBE-2) in air and vacuum ambiences. (b) The typical dark current response curve measured at repeated exposure to pure oxygen and vacuum for the MBE-GaN NWs.

for photoconduction between the different NW materials.[50] Accordingly, Γ_n can be the index determining the intrinsic PC efficiency based on the material's point of view. Calculation of Γ_n can be made by the equation.[46–48]

$$\Gamma_n = \eta\tau\mu = \eta\frac{\Gamma}{(V/l^2)} = \frac{E}{q}\frac{i_p}{P}\frac{l^2}{V}. \quad (2)$$

By ruling out the contributions of l and V from i_p in Fig. 4b, the Γ_n versus I for the different GaN NWs are shown in Fig. 4c. The Γ_n values of the MBE-grown GaN NW with short active region (l = 0.4 μm) and very high Γ ($\sim 10^8$) are also calculated and plotted for comparison adopting the i_p value in Ref. 28. From the result, the CVD-GaN NWs exhibit significantly higher Γ_n than the MBE ones by near two orders of magnitude. It is noted that the Γ_n of our MBE-GaN NWs located at 1.3–2.0 $\times$ 10^{-8} m^2 V^{-1} is close to the values of Ref. 28 in the same I range, indicating the consistent PC efficiency for the MBE-grown GaN NWs. The results indicate the CVD-NWs with superior intrinsic PC efficiency in comparison to the MBE ones.

Photoconduction Mechanism

The efficient photoconductivity in monocrystalline GaN NWs prepared by either CVD or MBE have been proposed to be originated from the electron–hole spatial separation induced by SBB.[25–33] The spatially separated transport of electron–hole pair (*ehp*) prolongs τ and thus enhances $\Gamma$and i_p. The SBB-controlled PC mechanism can be confirmed by the power dependence of τ or Γ_n. While the excitation power increases, the surface built-in potential or SBB will decrease due to the photovoltaic effect as shown in Fig. 5a. Reductions of the band slope (i.e. built-in electric field) and barrier height (ϕ_B) will increase the probability of electrons to overcome the barrier by thermionic emission (Fig. 5b) and increase recombination rate, and thus shorten τ. The mechanism will result in the sensitive power dependence of τ or Γ_n. According to the theoretical simulation and the experimental observation for the GaN epitaxial films[51,52] and NWs,[27,28,30,32] Γ_n (or Γ) follows an inverse power-law of $\Gamma_n \propto I^{-\kappa}$, where κ = 0.9–1.0. The CVD- and MBE-GaN NWs with κ values at 0.89 $\pm$ 0.01 and 0.79 $\pm$ 0.02, respectively, in Fig. 4c are consistent with the previous reports, indicating the SBB-controlled photoconductivity in this nitride nanostructure.

Temperature-Dependent Time-Resolved PC Measurement

According to the understanding, it is proposed that the difference of Γ_n between the CVD- and MBE-NWs could be attributed to the different barrier height (ϕ_B) and width (w) of surface depletion region (SDR). The higher ϕ_B, that suppresses electrons to overcome the barrier to recombine with holes and surface trap states by the thermionic emission, will induce a longer τ or higher Γ_n. Figure 6a depicts the time-resolved photocurrent decay measurement at the temperature T of 300 K for the CVD- and MBE-GaN NWs. The result shows the CVD-NW with higher Γ_n also exhibit a much longer decay time (τ_d) at ~6800 s than the MBE one ($\tau_d \sim$ 25 s). As τ_d with the physical meaning of electron lifetime in thermal equilibrium without light-flattening of SBB,[34] the longer τ_d of CVD-NWs actually agrees with the higher ϕ_B and stronger SBB in comparison to MBE-NWs.

As the recombination mechanism of spatially separated *ehp* in the GaN NWs is similar to the thermal activation of hole trapping in the GaN films,[53] the $q\phi_B$, which is assumed as the activation energy required to overcome the effective barrier, can be obtained by the temperature-dependent τ_d measurement. Figure 6b and c illustrates the normalized photocurrent decay curves measured at different temperature and in vacuum ambience ($\sim 10^{-4}$ torr) for the CVD -(sample# CVD-1) and MBE- (sample# MBE-2) GaN NWs, respectively. The results show the CVD-NW with much longer τ_d

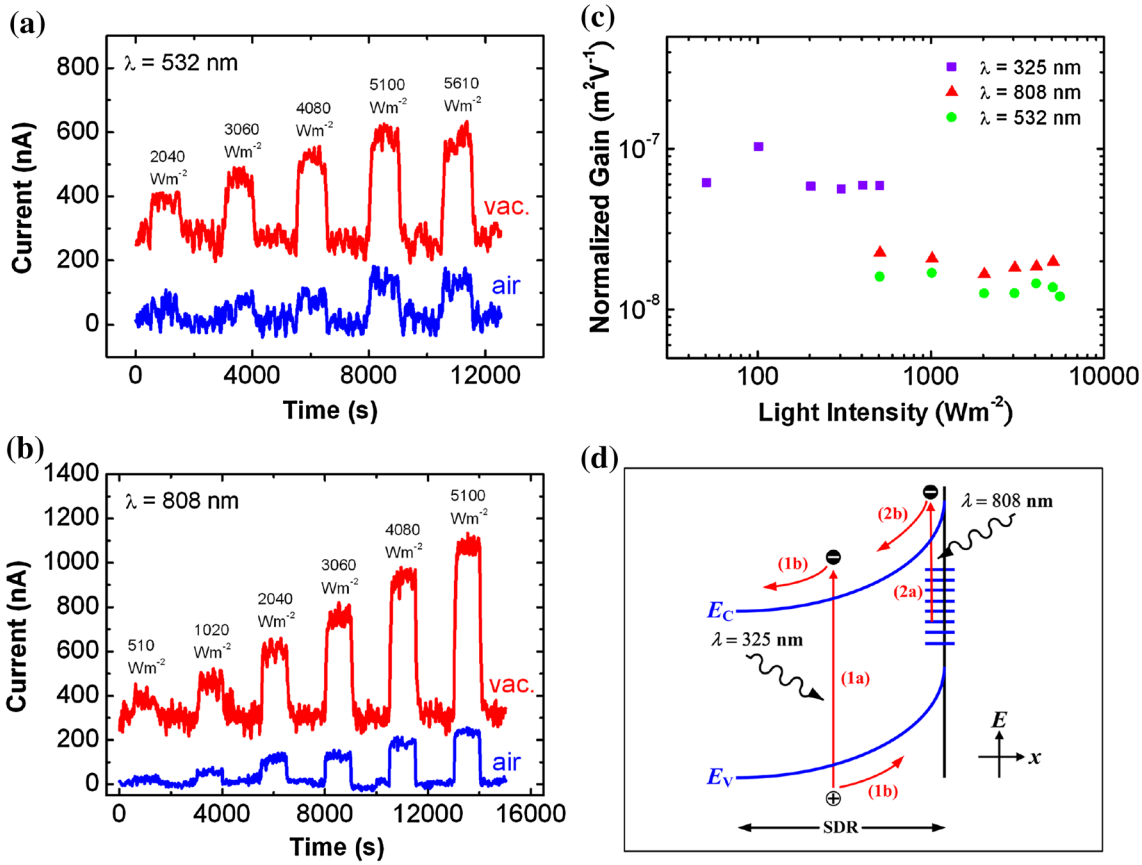

Fig. 8. (a) The photocurrent response curves under the sub-bandgap excitations at (a) λ = 532 nm and (b) λ = 808 nm at different light intensities for the MBE-GaN NWs (sample#MBE-2) in air and vacuum ambiences. (c) The normalized gain versus light intensity curves for the MBE-GaN NWs (sample#MBE-2) under different excitation wavelengths (λ) at 325, 532 nm and 808 nm measured in vacuum ambience. (d) The schematic PC processes for the GaN NWs under (1) inter-bandgap and (2) sub-bandgap excitations. Step (1a): Electron–hole pair is generation by inter-bandgap excitation (λ = 325 nm) in the surface depletion region (SDR); Step (1b): electron–hole spatial separation due to the surface band bending (SBB). Step (2a): electron is excited from the negatively charged surface state to the conduction band by sub-bandgap excitation (λ = 808 or 532 nm); Step (2b): excess electron moves to the core region due to the SBB. The recombination will only take place when electron overcomes the barrier of SBB and is recaptured by the surface states.

and more significant temperature dependence in comparison to the MBE-NW. By the Arrhenius plots for the fitted τ_d versus T (Fig. 6d), the ϕ_B can be obtained according to $\tau_d(T) \propto \exp(q\phi_B/kT)$.[53] The result shows the CVD-NWs with the ϕ_B at 160 ± 30 mV which is much higher than that of the MBE-NWs (ϕ_B = 20 ± 2 mV). The result also confirmed the longer τ_d or higher Γ_n for the CVD-NWs is originated from the higher ϕ_B or stronger SBB.

In principle, formation of the depletion region induced by surface states in n-type semiconductors follows the similar model as the depleted n region in a p^+n or Schottky diode. So, the relationship of ϕ_B and carrier concentration (n) will follow $\phi_B \propto \ln(n/n_i)$, where n_i is the intrinsic carrier concentration.[50,54] As MBE performs at ultra-high vacuum condition, the growth can usually provide a better control of the impurity/defect density than the CVD approach. According to the literature, the n values of MBE-GaN NWs are in the range of 1×10^{17} cm^{-3} to 6×10^{17} cm^{-3},[25,28] which is over one order of magnitude lower than that ($n = 5 \times 10^{18}$–5×10^{20} cm^{-3}) of the CVD ones.[29,55,56] By adopting the n values, the ratio of $\phi_B^{CVD}/\phi_B^{MBE}$ is about 1.03–1.14. Although the higher n corresponds to a higher ϕ_B for the CVD-GaN NWs, which is consistent with the experimental results. It is noted that the theoretical ratio is much smaller than the experimental value at 8 ($\phi_B^{CVD}/\phi_B^{MBE}$ = 160 meV/20 meV) obtained by the temperature-dependent τ_d measurement. While only considering the n difference and taking the value of ϕ_B^{CVD} = 160 mV, the calculated ϕ_B^{MBE} will be 140–155 mV, which is also much higher than the experimental value at 20 mV.

As the aforementioned discussion is on the basis of the same surface state density and different n in the CVD- and MBE-GaN NWs, the realistic case could deviate from the assumption. The MBE-NWs with the long-axis along ⟨001⟩ (c-axial) orientation is different from the ⟨1$\bar{1}$0⟩ (m-axial) CVD-NWs. The c-plane has been known as a strong polar surface compared to the non-polar m or a-plane in this III-nitride semiconductor. The c-axial NWs without the side wall of the c-plane could exhibit the non-polar characteristic, which is different from the polar m-axial NWs. In addition, the surface polarity

has been attributed to be one of the origins leading to SBB.[57–59] The polar surface with favorable oxygen adsorption or native oxide formation that enhances band bending has also been confirmed in the GaN epitaxial films.[60–63] Accordingly, it is inferred that the non-polar MBE-GaN NWs may have a much lower charged surface state density than the polar CVD ones. The limited density of surface state in MBE-NWs is not sufficient to capture numerous electrons and to produce dense space changes in SDR. The difference of surface character or axial orientation could make the practical ϕ_B value much lower than the theoretical estimation in the MBE-GaN NWs.

In addition to the difference in axial orientation and surface polarity, the use of a metal catalyst could also result in the different transport properties in GaN NWs. As Au could act as a donor dopant[64] and was used as the catalysts for CVD growth, the inevitable incorporation of Au atom into GaN NWs could give rise to an additional doping. In addition, the CVD growth at relatively higher background pressure (10^{-3}–10^{-5} torr) in comparison to MBE (10^{-9}–10^{-10} torr) implies that the CVD-GaN NWs could also have higher oxygen (donor) incorporation. The fundamental differences of CVD and MBE growth indicate the probably higher extra doping concentration and defect density in CVD-NWs. The inference is actually consistent with the previous reports in which the CVD-GaN NWs usually have higher carrier concentration ($n = 5 \times 10^{18}$–5×10^{20} cm^{-3})[29,55,56] than that of the MBE ones ($n = 1 \times 10^{17}$–6×10^{17}).[25,28] Because higher n and defect density can induce higher SBB and decrease the band-to-band recombination probability, respectively, the growth approach could also be responsible for the differences of the PC and PL characteristics.

It is noted that the CVD-GaN NWs exhibit more efficient photoconductivity than the MBW ones, which is opposite to the viewpoint of the material quality. The PL examination has pointed out the superior structural quality and less defect density for the MBE-NWs compared with the CVD ones. But the relatively defective CVD-NWs exhibit higher photocurrent generation efficiency instead. The opposite trend between the PL and PC performances is somewhat unexpected from the bulk semiconductor's point of view. Nevertheless, the interesting difference actually reflects the nature of surface-controlled PC and bulk-dominant PL in the GaN NWs. The photoconductivity relies upon the densities of surface states and bulk donor defects, but, on the contrary, these surface and bulk defects hamper the luminescence of the nitride nanostructure.

Ambience-Dependent Photoconductivity Under Sub-bandgap Excitation

Finally, the surface-dominant photoconductivity in MBE-GaN NWs was also found to be sensitive to the ambient environment. Figure 7a depicts the photocurrent responses to the illumination at $\lambda = 325$ nm and $I = 510$ W m^{-2} for the MBE-GaN NWs (sample#MBE-2) in air and vacuum ambiences. The result shows that the photocurrent was substantially enhanced by changing the ambience from air to vacuum. Because the photocurrent is controlled by the SBB, the result implies that oxygen adsorption could release the electrons trapped by the surface states and lower SBB. The enhanced photocurrent in vacuum is somewhat similar to that in metal oxide semiconductor NWs such as ZnO and TiO_2,[48,65] the only difference is that the foreign oxygen molecules prefer capturing electrons in the surface as an acceptor-like state. To confirm the role of oxygen, dark current response was measured by the repeated exposure to pure oxygen and vacuum for the MBE-GaN NWs as shown in Fig. 7b. The result shows that the dark current increases at oxygen exposure environment, which manifests the oxygen molecule acts as a donor-like state by releasing trapped electron in the surface and increases carrier concentration in this intrinsically n-type semiconductor. As the similar observation was also reported for the CVD-GaN NWs,[34] the results indicate the GaN NWs with c-axial and m-axial long axes have the oxygen effect in common.

In addition, photocurrent enhancements in vacuum were also observed by sub-bandgap excitation at $\lambda = 532$ nm and 808 nm for the MBE-GaN NW (sample#MBE-2) as shown in Fig. 8a and b, respectively. Usually, higher light intensities ($I > 500$ W m^{-2}) are required to generate observable photocurrent by the sub-bandgap excitation. Figure 8c depicts the calculated Γ_n values for the 325-nm, 532-nm and 808-nm excitations in vacuum ambience for comparison. The result shows the Γ_n values ($7.5 \pm 2.5 \times 10^{-8}$ m^2 V^{-1}) under the inter-bandgap excitation are higher than those ($1.7 \pm 0.5 \times 10^{-8}$ m^2 V^{-1}) under the sub-bandgap excitation by a factor of four. Because the sub-bandgap photoconductivity also exhibits environment dependence, the result implies that the photocarriers are predominantly excited from the surface states to the conduction band. The surface-generated electrons in the conduction band will follow a similar spatial separation mechanism as these generated in the SDR by inter-bandgap excitation. The recombination takes place when excess electrons overcome the barrier of SBB and are recaptured by the surface state. Accordingly, the electron lifetime and photocurrent at 532-nm and 808-nm excitations are also dependent on the SBB and can be increased in vacuum due to the increase of SBB. The aforementioned PC processes are schematically illustrated in Fig. 8d. As the absorption is limited to the surface at sub-bandgap excitation, it can be expected that the number of carrier generation is much lower than the SDR absorption in the bulk at inter-bandgap excitation. The lower quantum efficiency can explain why the 532-nm and 808-nm illuminations with lower Γ_n values in comparison to the 325-nm excitation.

CONCLUSION

The comparison of the CVD- and MBE-grown GaN NWs have been made based on the properties of structure, PL, and PC. The structural characterizations by XRD, Raman scattering, HRTEM, and SAD show the common single-crystalline quality but different long-axial orientations of the CVD- and MBE-GaN NWs. However, the PL measurement points out the better band-edge emission and much less defect density in the MBE-NWs compared to those of the CVD ones. The investigation of the PC efficiency further indicates an interesting fact that the relatively defective CVD-GaN NWs exhibit better photocurrent generation and carrier collection efficiency. The interesting difference between the PL and PC can be realized by the respective bulk and surface-dominant mechanisms in this nitride 1D nanostructure.

ACKNOWLEDGEMENTS

The author R.S.C. would like to thank the financial support of the Taiwan National Science Council (Grant No. NSC 99-2112-M-011-001-MY3 and NSC 99-2738-M-011-001) and the National Taiwan University of Science and Technology (NTUST).

REFERENCES

1. H.X. Jiang and J.Y. Lin, *Crit. Rev. Solid State Mater. Sci.* 28, 131 (2003).
2. S. Chattopadhyay, A. Ganguly, K.H. Chen, and L.C. Chen, *Crit. Rev. Solid State Mater. Sci.* 34, 224 (2009).
3. Y. Li, F. Qian, J. Xiang, and C.M. Lieber, *Mater. Today* 9, 18 (2006).
4. R.S. Chen, A. Ganguly, L.C. Chen, and K.H. Chen, *GaN and ZnO-based Materials and Devices*, ed. S. Pearton (Berlin: Springer, 2012), p. 295.
5. G. Cheng, A. Kolmakov, Y. Zhang, M. Moskovits, R. Munden, M.A. Reed, G. Wang, D. Moses, and J. Zhang, *Appl. Phys. Lett.* 83, 1578 (2003).
6. Y. Li, J. Xiang, F. Qian, S. Gradecak, Y. Wu, H. Yan, D.A. Blom, and C.M. Lieber, *Nano Lett.* 6, 1468 (2006).
7. H.M. Kim, Y.H. Cho, H. Lee, S.I. Kim, S.R. Ryu, D.Y. Kim, T.W. Kang, and K.S. Chung, *Nano Lett.* 4, 1059 (2004).
8. S. Han, W. Jin, D. Zhang, T. Tang, C. Li, X. Liu, Z. Liu, B. Lei, and C. Zhou, *Chem. Phys. Lett.* 389, 176 (2004).
9. R.S. Chen, S.W. Wang, Z.H. Lan, J.T.H. Tsai, C.T. Wu, L.C. Chen, K.H. Chen, Y.S. Huang, and C.C. Chen, *Small* 4, 925 (2008).
10. C.P. Chen, A. Ganguly, C.H. Wang, C.W. Hsu, S. Chattopadhyay, Y.K. Hsu, Y.C. Chang, K.H. Chen, and L.C. Chen, *Anal. Chem.* 81, 36 (2009).
11. Y. Dong, B. Tian, T.J. Kempa, and C.M. Lieber, *Nano Lett.* 9, 2183 (2009).
12. S. Nakamura, S. Pearton, and G. Fasol, *The Blue Laser Diode: The Complete Story* (Berlin: Springer, 2000).
13. H. Morkoc, *Nitride Semiconductors and Devices* (Berlin: Springer, 1999).
14. B. Monemar, *J. Mater. Sci.: Mater. Electron.* 10, 227 (1999).
15. K. Kubota, Y. Kobayashi, and K. Fujimoto, *J. Appl. Phys.* 66, 2984 (1989).
16. J.W. Orton and C.T. Foxon, *Rep. Prog. Phys.* 61, 1 (1998).
17. S.A. Jewett, M.S. Makowski, B. Andrews, M.J. Manfra, and A. Ivanisevic, *Acta Biomater.* 8, 728 (2012).
18. T. Kuykendall, P. Pauzauskie, S.K. Lee, Y.F. Zhang, J. Goldberger, and P.D. Yang, *Nano Lett.* 3, 1063 (2003).
19. T. Kuykendall, P.J. Pauzauskie, Y.F. Zhang, J. Goldberger, D. Sirbuly, J. Denlinger, and P.D. Yang, *Nat. Mater.* 3, 524 (2004).
20. C.C. Chen, C.C. Yeh, C.H. Chen, M.Y. Yu, H.L. Liu, J.J. Wu, K.H. Chen, L.C. Chen, J.Y. Peng, and Y.F. Chen, *J. Am. Chem. Soc.* 123, 2791 (2001).
21. R. Meijers, T. Richter, R. Calarco, T. Stoica, H.P. Bochem, M. Marso, and H. Luth, *J. Cryst. Growth* 289, 381 (2006).
22. K.A. Bertness, A. Roshko, N.A. Sanford, J.M. Barker, and A.V. Davydov, *J. Cryst. Growth* 287, 522 (2006).
23. J. Ristic, E. Calleja, S. Fernandez-Garrido, L. Cerutti, A. Trampert, U. Jahn, and K.H. Ploog, *J. Cryst. Growth* 310, 4035 (2008).
24. Y.T. Chen, W.C. Tsai, W.Y. Chen, C.L. Hsiao, H.C. Hsu, W.H. Chang, T.M. Hsu, K.H. Chen, and L.C. Chen, *Opt. Exp.* 20, 16166 (2012).
25. R. Calarco, M. Marso, T. Richter, A.I. Aykanat, R. Meijers, T. Stoica, and H. Luth, *Nano. Lett.* 5, 981 (2005).
26. R. Calarco, T. Stoica, O. Brandt, and L. Geelhaar, *J. Mater. Res.* 26, 2157 (2011).
27. R.S. Chen, H.Y. Chen, C.Y. Lu, K.H. Chen, C.P. Chen, L.C. Chen, and Y.J. Yang, *Appl. Phys. Lett.* 91, 223106 (2007).
28. F. Gonzalez-Posada, R. Songmuang, M. Den Hertog, and E. Monroy, *Nano Lett.* 12, 172 (2012).
29. H.Y. Chen, R.S. Chen, F.C. Chang, L.C. Chen, K.H. Chen, and Y.J. Yang, *Appl. Phys. Lett.* 95, 143123 (2009).
30. H.Y. Chen, R.S. Chen, N.K. Rajan, F.C. Chang, L.C. Chen, K.H. Chen, Y.J. Yang, and M.A. Reed, *Phys. Rev. B* 84, 205443 (2011).
31. N.A. Sanford, L.H. Robins, P.T. Blanchard, K. Soria, B. Klein, B.S. Eller, K.A. Bertness, J.B. Schlager, and A.W. Sanders, *J. Appl. Phys.* 113, 174306 (2013).
32. R.S. Chen, H.Y. Tsai, Y.S. Huang, Y.T. Chen, L.C. Chen, and K.H. Chen, *Appl. Phys. Lett.* 101, 113109 (2012).
33. N.A. Sanford, P.T. Blanchard, K.A. Bertness, L. Mansfield, J.B. Schlager, A.W. Sanders, A. Roshko, B.B. Burton, and S.M. George, *J. Appl. Phys.* 107, 034318 (2010).
34. R.S. Chen, C.Y. Lu, K.H. Chen, and L.C. Chen, *Appl. Phys. Lett.* 95, 233119 (2009).
35. A. Ganguly, C.P. Chen, Y.T. Lai, C.C. Kuo, C.W. Hsu, K.H. Chen, and L.C. Chen, *J. Mater. Chem.* 19, 928 (2009).
36. C.P. Chen, A. Ganguly, C.Y. Lu, T.Y. Chen, C.C. Kuo, R.S. Chen, W.H. Tu, W.B. Fischer, K.H. Chen, and L.C. Chen, *Anal. Chem.* 83, 1938 (2011).
37. C.Y. Chang, G.C. Chi, W.M. Wang, L.C. Chen, K.H. Chen, F. Ren, and S.J. Pearton, *J. Electro. Mater.* 35, 738 (2006).
38. C.Y. Nam, J.Y. Kim, and J.E. Fischer, *Appl. Phys. Lett.* 86, 193112 (2005).
39. T. Azuhata, T. Sota, K. Suzuki, and S. Nakamura, *J Phys* 7, L129 (1995).
40. L. Filippidis, H. Siegle, A. Hoffmann, C. Thomsen, K. Karch, and F. Bechstedt, *Phys. Status Solidi B* 198, 621 (1996).
41. V.Yu. Davydov, Yu.E. Kitaev, I.N. Goncharuk, A.N. Smirnov, J. Graul, O. Semchinova, D. Uffmann, M.B. Smirnov, A.P. Mirgorodsky, and R.A. Evarestov, *Phys. Rev. B* 58, 12899 (1998).
42. H.L. Liu, C.C. Chen, C.T. Chia, C.C. Yeh, C.H. Chen, M.Y. Yu, S. Keller, and S.P. DenBaars, *Chem. Phys. Lett.* 345, 245 (2001).
43. P. Bhattacharya, *Semiconductor Optoelectronic Devices* (Prentice-Hall Inc., New Jersey). *Chap.* 8, 346–351 (1997).
44. M. Razeghi and A. Rogalski, *J. Appl. Phys.* 79, 7433 (1996).
45. R.S. Chen, H.Y. Chen, C.Y. Lu, K.H. Chen, C.P. Chen, L.C. Chen, and Y.J. Yang, *Appl. Phys. Lett.* 91, 223106 (2007).
46. J.D. Prades, R. Jimenez-Diaz, F. Hernandez-Ramirez, L. Fernandez-Romero, T. Andreu, A. Cirera, A. Romano-Rodriguez, A. Cornet, J.R. Morante, S. Barth, and S. Mathur, *J. Phys. Chem. C* 112, 14639 (2008).
47. C. Fabrega, F. Hernandez-Ramirez, J.D. Prades, R. Jimenez-Diaz, T. Andreu, and J.R. Morante, *Nanotechnology* 21, 445703 (2010).
48. R.S. Chen, C.A. Chen, H.Y. Tsai, W.C. Wang, and Y.S. Huang, *J. Phys. Chem. C* 116, 4267 (2012).
49. R.H. Bube, *Photoconductivity of Solids* (John Wiley & Sons, New York, 1960) Chap. 3, pp. 59-60.
50. R.S. Chen, W.C. Wang, M.L. Lu, Y.F. Chen, H.C. Lin, K.H. Chen, and L.C. Chen, *Nanoscale* 5, 6867 (2013).

51. E. Munoz, E. Monroy, J.A. Garrido, I. Izpura, F.J. Sanchez, M.A. Sanchez-Garcia, E. Calleja, B. Beaumont, and P. Gibart, *Appl. Phys. Lett.* 71, 870 (1997).
52. J.A. Garrido, E. Monroy, I. Izpura, and E. Munoz, *Semicond. Sci. Technol.* 13, 563 (1998).
53. H.M. Chen, Y.F. Chen, M.C. Lee, and M.S. Feng, *J. Appl. Phys.* 82, 899 (1997).
54. D.A. Neamen, *Semiconductor Physics and Devices: Basic Principles*, 3rd edition (McGraw-Hill Inc., New York, 2003) Chap. 4, pp. 106-112; Chap. 7, 241.
55. B.S. Simpkins, M.A. Mastro, C.R. Eddy Jr., and P.E. Pehrsson., *J. Appl. Phys.* 103, 104313 (2008).
56. E. Stern, G. Cheng, E. Cimpoiasu, R. Klie, S. Guthrie, J. Klemic, I. Kretzschmar, E. Steinlauf, D. Turner-Evans, E. Broomfield, J. Hyland, R. Koudelka, T. Boone, M. Young, A. Sanders, R. Munden, T. Lee, D. Routenberg, and M.A. Reed, *Nanotechnology* 16, 2941 (2005).
57. S.A. Chevtchenko, M.A. Reshchikov, Q. Fan, X. Ni, Y.T. Moon, A.A. Baski, and H. Morkoc, *J. Appl. Phys.* 101, 113709 (2007).
58. K.M. Jones, P. Visconti, F. Yun, A.A. Baski, and H. Morkoc, *Appl. Phys. Lett.* 78, 2497 (2001).
59. B.J. Rodriguez, W.C. Yang, R.J. Nemanich, and A. Gruverman, *Appl. Phys. Lett.* 86, 112115 (2005).
60. M.A. Garcia, S.D. Wolter, T.H. Kim, S. Choi, J. Baier, A. Brown, M. Losurdo, and G. Bruno, *Appl. Phys. Lett.* 88, 013506 (2006).
61. H. Ishikawa, S. Kobayashi, Y. Koide, S. Yamasaki, S. Nagai, J. Umezaki, M. Koike, and M. Murakami, *J. Appl. Phys.* 81, 1315 (1997).
62. C.I. Wu, A. Kahn, N. Taskar, D. Dorman, and D. Gallagher, *J. Appl. Phys.* 83, 4249 (1998).
63. T.K. Zywietz, J. Neugebauer, and M. Scheffler, *Appl. Phys. Lett.* 74, 1695 (1999).
64. J.A. Chisholm and P.D. Bristowe, *Modelling Simul. Mater. Sci. Eng.* 9, 249 (2001).
65. C. Soci, A. Zhang, B. Xiang, S.A. Dayeh, D.P.R. Aplin, J. Park, X.Y. Bao, Y.H. Lo, and D. Wang, *Nano Lett.* 7, 1003 (2007).